

## Article

# Effects of Silica Shell Encapsulated Nanocrystals on Active $\chi$ -Fe<sub>5</sub>C<sub>2</sub> Phase and Fischer–Tropsch Synthesis

Seunghee Cha <sup>1</sup>, Heewon Kim <sup>1</sup>, Hyunkyung Choi <sup>2</sup>, Chul Sung Kim <sup>2</sup> and Kyoung-Su Ha <sup>1,\*</sup>

<sup>1</sup> Department of Chemical and Biomolecular Engineering, Sogang University, 35 Baekbeom-ro, Mapo-gu, Seoul 04107, Korea

<sup>2</sup> Department of Physics, Kookmin University, 77 Jeongneung-ro, Seongbuk-gu, Seoul 02707, Korea

\* Correspondence: philoseus@sogang.ac.kr; Tel.: +82-2-3274-4859

**Abstract:** Among various iron carbide phases,  $\chi$ -Fe<sub>5</sub>C<sub>2</sub>, a highly active phase in Fischer–Tropsch synthesis, was directly synthesized using a wet-chemical route, which makes a pre-activation step unnecessary. In addition,  $\chi$ -Fe<sub>5</sub>C<sub>2</sub> nanoparticles were encapsulated with mesoporous silica for protection from deactivation. Further structural analysis showed that the protective silica shell had a partially ordered mesoporous structure with a short range. According to the XRD result, the sintering of  $\chi$ -Fe<sub>5</sub>C<sub>2</sub> crystals did not seem to be significant, which was believed to be the beneficial effect of the protective shell providing restrictive geometrical space for nanoparticles. More interestingly, the protective silica shell was also found to be effective in maintaining the phase of  $\chi$ -Fe<sub>5</sub>C<sub>2</sub> against re-oxidation and transformation to other iron carbide phases. Fischer–Tropsch activity of  $\chi$ -Fe<sub>5</sub>C<sub>2</sub> in this study was comparable to or higher than those from previous reports. In addition, CO<sub>2</sub> selectivity was found to be very low after stabilization.

**Keywords:** Fischer–Tropsch; iron carbide; encapsulation; ordered mesoporous silica



**Citation:** Cha, S.; Kim, H.; Choi, H.; Kim, C.S.; Ha, K.-S. Effects of Silica Shell Encapsulated Nanocrystals on Active  $\chi$ -Fe<sub>5</sub>C<sub>2</sub> Phase and Fischer–Tropsch Synthesis. *Nanomaterials* **2022**, *12*, 3704. <https://doi.org/10.3390/nano12203704>

Academic Editor: Raphaël Schneider

Received: 20 September 2022

Accepted: 10 October 2022

Published: 21 October 2022

**Publisher's Note:** MDPI stays neutral with regard to jurisdictional claims in published maps and institutional affiliations.



**Copyright:** © 2022 by the authors. Licensee MDPI, Basel, Switzerland. This article is an open access article distributed under the terms and conditions of the Creative Commons Attribution (CC BY) license (<https://creativecommons.org/licenses/by/4.0/>).

## 1. Introduction

Fischer–Tropsch synthesis (FTS) is known to be one of the most important reactions in gas-to-liquid processes since it produces synthetic oils and basic chemicals such as naphtha, gasoline, diesel, waxy products, ethylene, and propylene [1–3]. Among the FTS catalysts, iron-based catalysts are attracting more attraction due to their low cost and flexibility of operation to yield various kinds of products [4–6]. There have been many research articles dealing with iron carbide phases as the active phases of Fischer–Tropsch synthesis.  $\chi$ -Fe<sub>5</sub>C<sub>2</sub> is usually considered to be one of the most active phases [4,7]. However, the  $\chi$ -Fe<sub>5</sub>C<sub>2</sub> phase has been known susceptible to significant phase transformation to other carbides or oxide phases during reaction [8,9]. Despite the effort to protect and decrease the changing rate in phases, a K-promoted Fe catalyst showed a transition from the  $\chi$ -Fe<sub>5</sub>C<sub>2</sub> phase into the  $\epsilon'$ -Fe<sub>2.2</sub>C phase [10], which is also known as an active phase for FTS. It was reported that the growth of an amorphous carbon layer formed around the catalyst particle was attributed to the resistance against re-oxidation and had an influence on the phase change between active iron carbide phases. Despite the beneficial feature of resistance against re-oxidation, the gradual decrease in conversion was not avoided, and the original phase did not seem to be well protected either.

Regarding the formation degree of iron carbides when using syngas as an activation gas [11–13], it was reported that a decrease in H<sub>2</sub>/CO ratio during the pre-activation process could facilitate carburization to give more active iron carbides [14]. According to Smit et al. [15], thermodynamics with chemical potential could explain the formations of  $\chi$ -Fe<sub>5</sub>C<sub>2</sub>,  $\theta$ -Fe<sub>3</sub>C, Fe<sub>7</sub>C<sub>3</sub>, and  $\epsilon$ -carbides and their relative stabilities. They also argued that the catalyst composed mainly of the  $\chi$ -Fe<sub>5</sub>C<sub>2</sub> phase prepared under high chemical potential was found to be quite vulnerable to oxidation during FTS because the amorphous iron carbides in the catalyst appeared to be oxidized to iron oxide crystals while the intensity of

the  $\chi$ -Fe<sub>5</sub>C<sub>2</sub> phase in the XRD spectrum remained unchanged. As far as the formation of the  $\chi$ -Fe<sub>5</sub>C<sub>2</sub> phase is concerned, a wet-chemical synthesis was introduced [8], and it produced a pure  $\chi$ -Fe<sub>5</sub>C<sub>2</sub> phase only, by forming octadecylamine and a Fe carbonyl complex followed by carburization with C<sub>2</sub>–C<sub>3</sub> molecules from thermally fragmented octadecylamine at around 350 °C, and the procedure and process of synthesis were reconstructed in a later study [16]. These authors argued that the phase change of  $\chi$ -Fe<sub>5</sub>C<sub>2</sub> phase to iron oxide was ascribed to the cause of deactivation instead of hydrocarbon shielding during FTS. Tang et al. reported that  $\chi$ -Fe<sub>5</sub>C<sub>2</sub> phase nanoparticles synthesized by a wet-chemical route might be more vulnerable to re-oxidation during a reaction than iron carbides prepared by gas pre-treatment [17]. Regarding the  $\chi$ -Fe<sub>5</sub>C<sub>2</sub> phase, a highly active carbide phase was reported to be prepared by infiltration of the iron precursor melt into graphene flakes. The resulting catalyst was found to have a highly active  $\chi$ -Fe<sub>5</sub>C<sub>2</sub> phase in terms of total CO conversion at high space velocity, whereas CO to CO<sub>2</sub> conversion was also very high and comparable to CO to hydrocarbon conversion [18]. To protect against sintering, core–shell-like catalyst particles were developed and Co<sub>3</sub>O<sub>4</sub>@SiO<sub>2</sub> was prepared and tested for FTS [19]. It was reported that enlarging the pore size of the shell could increase the dispersion of active core particles and catalytic performance as well. In addition, the encapsulation improved catalytic stability.

In this study,  $\chi$ -Fe<sub>5</sub>C<sub>2</sub> phase nanoparticles were prepared to elucidate the performance of pure  $\chi$ -Fe<sub>5</sub>C<sub>2</sub> instead of a mixture of iron carbides. By encapsulating the nanoparticle with a partially ordered mesoporous silica shell, the effects of the protective shell on sintering and re-oxidation of  $\chi$ -Fe<sub>5</sub>C<sub>2</sub> were investigated by XRD, TEM with SAED, physisorption, and other methods. In addition, the catalytic performance was tested and compared with the performances of catalysts having different and mixed iron carbides.

## 2. Materials and Methods

### 2.1. Materials

The octadecylamine (85% purity), iron pentacarbonyl (Fe(CO)<sub>5</sub>, 99.99% purity), polyvinylpyrrolidone (PVP, average MW = 40,000), triethanolamine (TEA, 98% purity), and tetraethyl orthosilicate (TEOS, 98% purity) were purchased from Sigma Aldrich, Burlington, MA, USA. The hexadecyltrimethylammonium bromide (CTAB) was purchased from TCI Chemicals, Tokyo, Japan. All chemicals were used without further purification.

### 2.2. Catalyst Preparation

#### 2.2.1. Synthesis of $\chi$ -Fe<sub>5</sub>C<sub>2</sub> Nanoparticles

Iron carbide nanoparticle preparation was conducted as follows: The  $\chi$ -Fe<sub>5</sub>C<sub>2</sub> nanoparticles were synthesized via a wet-chemical route [16]. First, 30 g of octadecylamine and 0.226 g of CTAB were introduced into a 3-neck round bottom flask and degassed with inert gas flow at room temperature. The synthesis of iron carbide nanoparticles proceeded under inert conditions during the whole procedure. Consistent N<sub>2</sub> flow was connected to the mixture during the interval of the synthesis of iron carbide nanoparticles. Then the mixture was heated to 120 °C. When octadecylamine and CTAB were fully mixed, 1 mL of iron pentacarbonyl (Fe(CO)<sub>5</sub>) was added into the mixture, which was heated to 180 °C and maintained for 30 min, followed by being heated to 350 °C and maintained for 5 min. Thereafter, the mixture was cooled to room temperature, and passivation was conducted for 15 min using a 5% O<sub>2</sub>/N<sub>2</sub> mixture flow. The mixture was then dispersed in hexane and washed several times. During the wash, magnets were used for the separation of the  $\chi$ -Fe<sub>5</sub>C<sub>2</sub> nanoparticles having magnetic properties. The washing temperature was room temperature, and about 1 min of washing with hexane was repeated around 20 times until the separation of iron carbide nanoparticles. About 250 mL of hexane was needed for the repetitive separation process.

### 2.2.2. Synthesis of $\chi$ -Fe<sub>5</sub>C<sub>2</sub>@SiO<sub>2</sub> Catalysts

First, 0.07 g of  $\chi$ -Fe<sub>5</sub>C<sub>2</sub> nanoparticles was mixed with 3 g of polyvinylpyrrolidone (PVP) in 50 mL of ethanol to meet the final weight percent, and PVP-protected  $\chi$ -Fe<sub>5</sub>C<sub>2</sub> nanoparticles were dispersed in ethanol by sonication. This mixture was named solution A. Encapsulation of iron carbide nanoparticles with silica was conducted as follows: First, 8.4 g of CTAB and 72 g of deionized water were mixed at 60 °C for 30 min using a rotary mixer, and solution A was added dropwise and mixed. This mixture was mixed at 60 °C for at least 30 min and named solution B. At the same time, solution C was prepared by mixing 6 g of tetraethyl orthosilicate (TEOS) and 45 g of triethanolamine (TEA) in a Teflon-lined stainless-steel autoclave, and hydrothermal synthesis was conducted at 90 °C for 20 min. Finally, solutions B and C were mixed after they had cooled to room temperature. The final mixture was mixed for 48 h using a rotating vessel. The mixture was then washed out with deionized water and ethanol and dried at 60 °C in a vacuum oven. The resulting samples were named  $\chi$ -Fe<sub>5</sub>C<sub>2</sub>@SiO<sub>2</sub>\_L. Through the reconstruction of the synthesis method,  $\chi$ -Fe<sub>5</sub>C<sub>2</sub>@SiO<sub>2</sub>\_H, which has higher Fe content than Fe<sub>5</sub>C<sub>2</sub>@SiO<sub>2</sub>\_L, was synthesized. The amounts of solution B and solution C were halved to increase Fe loading in catalysts. Considering the decreased amounts of solvent and solution, 0.13 g of  $\chi$ -Fe<sub>5</sub>C<sub>2</sub> nanoparticles was used in the case of the  $\chi$ -Fe<sub>5</sub>C<sub>2</sub>@SiO<sub>2</sub>\_H catalyst. In addition, the contact of PVP-protected  $\chi$ -Fe<sub>5</sub>C<sub>2</sub> nanoparticles with the aqueous solution was allowed only until the color of the mixture turned orange. The orange color indicated that the oxidation of  $\chi$ -Fe<sub>5</sub>C<sub>2</sub> nanoparticles occurred.  $\chi$ -Fe<sub>5</sub>C<sub>2</sub>@SiO<sub>2</sub>\_L (3.5 wt.%) and  $\chi$ -Fe<sub>5</sub>C<sub>2</sub>@SiO<sub>2</sub>\_H (12.2 wt.%) catalysts were synthesized in the same way, except the amounts of  $\chi$ -Fe<sub>5</sub>C<sub>2</sub> nanoparticles and the contact time of the nanoparticles and the aqueous solution were different.

### 2.3. Catalyst Characterization

N<sub>2</sub>-physisorption analysis was conducted using an ASAP 2020 analyzer (Micromeritics, Inc., Norcross, GA, USA) at −196 °C. Prior to the physisorption measurements, the samples were degassed at 150 °C for 12 h under vacuum condition. X-ray diffraction (XRD) analysis was performed using a Rigaku SmartLab with a D/teX Ultra 250 X-ray diffractometer with Cu K $\alpha$  radiation ( $\lambda = 0.154$  nm, 40 kV, 40 mA) at  $2\theta$  ranging from 10° to 65° for all samples. Small-angle X-ray scattering (SAXS) was conducted on an Empyrean with ScatterX78 PANalytical using 45 kV and 40 mA. A JEM-2100F high-resolution transmission electron microscope was used to obtain TEM images and SAED patterns, and the working voltage was 200 kV. X-ray photoelectron spectroscopy (XPS) was conducted using a K-Alpha X-ray Photoelectron Spectrometer System (Thermo Fisher Scientific Inc., Waltham, Massachusetts, USA). Prior to analysis, fresh and spent catalysts were pressed into thin pellets and etched with low-energy Ar ion irradiation for 400 s. During the experiments, a monochromatic Al K $\alpha$  (1486.6 eV) was adopted, and approximately 10<sup>−7</sup> Pa of vacuum condition was preserved. The correction of binding energy (BE) was performed referencing the BE of C 1s (284.6 eV). Inductively coupled plasma optical emission spectroscopy (ICP-OES) was performed using a Thermo Scientific iCAP 7000 to verify the content of iron in the catalyst samples. Thermogravimetric analysis (TGA) was performed with a Q50 instrument (TA Instruments) to identify the change in the silica pore structure of the fresh catalyst. The catalyst was heated under N<sub>2</sub> flow from 110 °C to 950 °C at a ramping rate of 20 °C/min. Fourier transform infrared (FT-IR) data were collected with a Thermo Nicolet iS50 FT-IR spectrometer (Thermo Fisher Scientific Inc., Waltham, MA, USA) forming a KBr pellet. A Mössbauer spectrometer of the electromechanical type with a <sup>57</sup>Co source in a Rh matrix was used in the constant-acceleration mode. The spectrometer was calibrated by collecting the Mössbauer spectra of a standard  $\alpha$ -Fe foil at room temperature. To produce a uniform thickness over the area of the Mössbauer absorber, each sample was clamped between two beryllium disks of 0.005-inch thickness and 1-inch diameter. The Mössbauer spectra were fitted by the least-squares method and provided the hyperfine field ( $H_{hf}$ ), isomer shift ( $\delta$ ), electric quadrupole splitting ( $\Delta E_Q$ ), and relative area of Fe.

## 2.4. Catalyst Evaluation

The Fischer–Tropsch activity test of the catalysts was conducted using a laboratory-scaled micro fixed-bed reactor system. For the reaction, 0.3 g of catalyst without dilution was loaded in the reactor. No pre-treatment steps were performed before the reaction, and syngas with a composition of  $\text{H}_2:\text{CO}:\text{CO}_2:\text{Ar} = 58.5:27.7:9.1:4.8$  was used. The reaction was conducted at a gas hourly space velocity (GHSV) of  $4000 \text{ mL/g}_{\text{cat}}/\text{h}$ . The reaction was conducted for 24 h, and the temperature and pressure were preserved at  $300^\circ\text{C}$  and 10 bar, respectively. The effluent from the reactor was analyzed using an on-line gas chromatograph (6500GC, Young Lin Instrument Co., Anyang, Korea) equipped with a thermal conductivity detector (TCD) and flame ionization detector (FID). A Carboxen 1000 packed column was used to detect Ar, CO,  $\text{CH}_4$ , and  $\text{CO}_2$ , and a GS-GASPRO capillary column was used to identify hydrocarbons.

## 3. Results and Discussion

### 3.1. Characterization of $\chi\text{-Fe}_5\text{C}_2$ Nanoparticles

After the synthesis of  $\chi\text{-Fe}_5\text{C}_2$  nanoparticles by the wet-chemical route, the average crystallite size and structure of the nanoparticles were investigated by XRD analysis. In Figure 1a, the X-ray diffraction pattern shows that only the  $\chi\text{-Fe}_5\text{C}_2$  phase (JCPDS No. 036-1248) existed in the nanoparticles. The average crystallite size was 20.50 nm, which was calculated using Scherrer's equation at  $2\theta = 39.4^\circ$ , and the peak was known as the (020) plane of  $\chi\text{-Fe}_5\text{C}_2$ . In addition, the broad peak that appeared in the range of  $2\theta = 16\text{--}33^\circ$  revealed the existence of amorphous carbon around the particles, as shown in Figure S1. TEM images of nanoparticles and their size distribution are shown in Figure 1b and its inset, respectively. Stochastic treatment indicated that the average particle size was observed as around 44 nm. The sizes of the nanoparticles were much larger than that of the crystallite observed by XRD. This is partly because the nanoparticles had polycrystalline characteristics, as shown in Figure 1c, and a similar result was also reported elsewhere [20]. As shown in Figure 1c, different lattices were observed and identified in one nanoparticle. A more detailed observation of the HRTEM image showed that the marked lattice distances of 0.208 nm and 0.239 nm indicated those of the (021) and (20-2) planes of the  $\chi\text{-Fe}_5\text{C}_2$  phase, respectively. In Figure 1d, the iron carbide phase was identified with SAED analysis, and only the  $\chi\text{-Fe}_5\text{C}_2$  phase was identified.

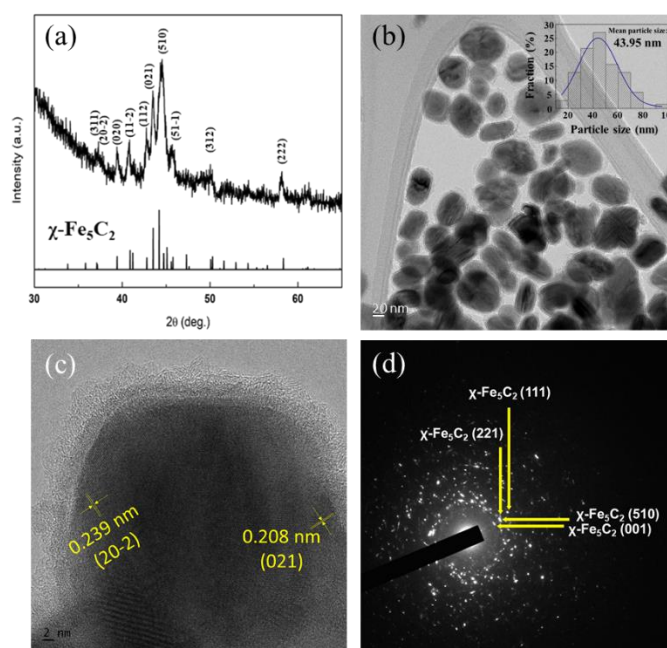


**Figure 1.** (a) XRD pattern; (b) TEM image; (c) HRTEM image; (d) SAED pattern of  $\chi\text{-Fe}_5\text{C}_2$  nanoparticles.

### 3.2. Morphology and Structure of Encapsulated Catalyst Particles $\chi$ -Fe<sub>5</sub>C<sub>2</sub>@SiO<sub>2</sub>

After the synthesis of silica-encapsulated catalysts, the structures of the  $\chi$ -Fe<sub>5</sub>C<sub>2</sub>@SiO<sub>2</sub>\_L and  $\chi$ -Fe<sub>5</sub>C<sub>2</sub>@SiO<sub>2</sub>\_H catalysts were examined and elucidated by XRD analysis. The X-ray diffraction spectrum of  $\chi$ -Fe<sub>5</sub>C<sub>2</sub>@SiO<sub>2</sub>\_L showed that the  $\chi$ -Fe<sub>5</sub>C<sub>2</sub> phase was not the only phase of iron in the catalyst, and peaks indicating  $\alpha$ -Fe<sub>2</sub>O<sub>3</sub> (JCPDS No. 33-0664) and  $\theta$ -Fe<sub>3</sub>C (JCPDS No. 35-0772) were found additionally, as shown in Figure 2. The step of encapsulating  $\chi$ -Fe<sub>5</sub>C<sub>2</sub> nanoparticles with a silica shell could be ascribed to the oxidation of iron carbide.  $\chi$ -Fe<sub>5</sub>C<sub>2</sub> as well as the amorphous iron carbide phase seemed to be oxidized in the first step of the encapsulation process, where nanoparticles were mixed with the aqueous solution at 60 °C for 30 min. Due to the relatively long duration of the first step, the oxidation state of iron species turned out to be  $\alpha$ -Fe<sub>2</sub>O<sub>3</sub> rather than Fe<sub>3</sub>O<sub>4</sub>. According to Tang et al.,  $\chi$ -Fe<sub>5</sub>C<sub>2</sub> nanoparticles synthesized by a wet-chemical route might be more vulnerable to re-oxidation during the reaction than iron carbides prepared by gas pre-treatment [17]. Therefore, we believed that the oxidation of  $\chi$ -Fe<sub>5</sub>C<sub>2</sub> nanoparticles occurred before the completion of the silica shell and oxidation took place in the middle of contact with the aqueous solution at 60 °C. We attempted to encapsulate iron carbide nanoparticles without compromising the active phase following a recipe from the literature [21], but this method proved unsuitable for us because of difficulties in dissolving and incorporating chemical agents such as CTAB and PVP.

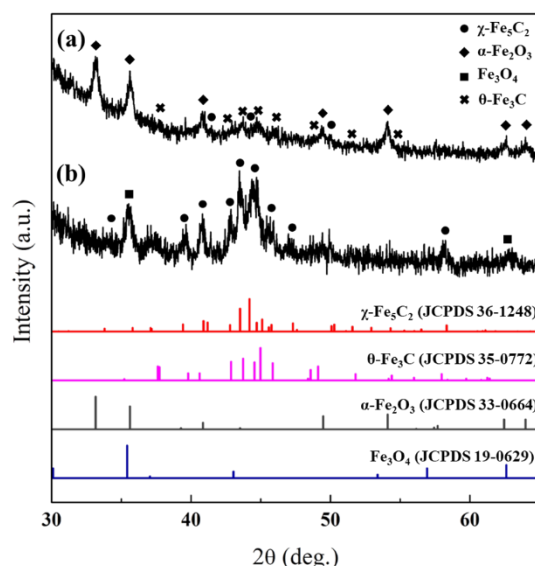


**Figure 2.** XRD pattern of fresh catalysts: (a)  $\chi$ -Fe<sub>5</sub>C<sub>2</sub>@SiO<sub>2</sub>\_L; (b)  $\chi$ -Fe<sub>5</sub>C<sub>2</sub>@SiO<sub>2</sub>\_H.

In order to suppress the phase change, the contact time with the aqueous solution mixture was decreased as much as possible when the  $\chi$ -Fe<sub>5</sub>C<sub>2</sub>@SiO<sub>2</sub>\_H catalyst was encapsulated with a silica shell. As a result, the XRD spectrum of Fe<sub>5</sub>C<sub>2</sub>@SiO<sub>2</sub>\_H exhibited the  $\chi$ -Fe<sub>5</sub>C<sub>2</sub> (JCPDS No. 36-1248) phase and the Fe<sub>3</sub>O<sub>4</sub> (JCPDS No. 19-0629) phase, which was a less oxidized phase than the  $\alpha$ -Fe<sub>2</sub>O<sub>3</sub> phase of the  $\chi$ -Fe<sub>5</sub>C<sub>2</sub>@SiO<sub>2</sub>\_L catalyst as mentioned above. The number of transformed phases and the degree of oxidation were found to be significantly reduced.

The morphology of the catalysts was investigated using TEM imaging analysis, and the results are shown in Figure 3. The size of the silica shells was approximately 100 nm in both catalysts, and the iron carbide nanoparticles were encapsulated as a core. The silica shell appeared spherical, and one or two  $\chi$ -Fe<sub>5</sub>C<sub>2</sub> nanoparticles appeared to be located inside the shell. In addition, spherical silica structures with diameters much smaller than 100 nm without nanoparticles inside were seen in both catalysts. By comparison between Figure 3b,f, it could be noticed that the  $\chi$ -Fe<sub>5</sub>C<sub>2</sub>@SiO<sub>2</sub>\_L catalyst contained more empty

silica structures than the  $\chi$ -Fe<sub>5</sub>C<sub>2</sub>@SiO<sub>2</sub>\_H catalyst, possibly due to the result of lower iron loading.

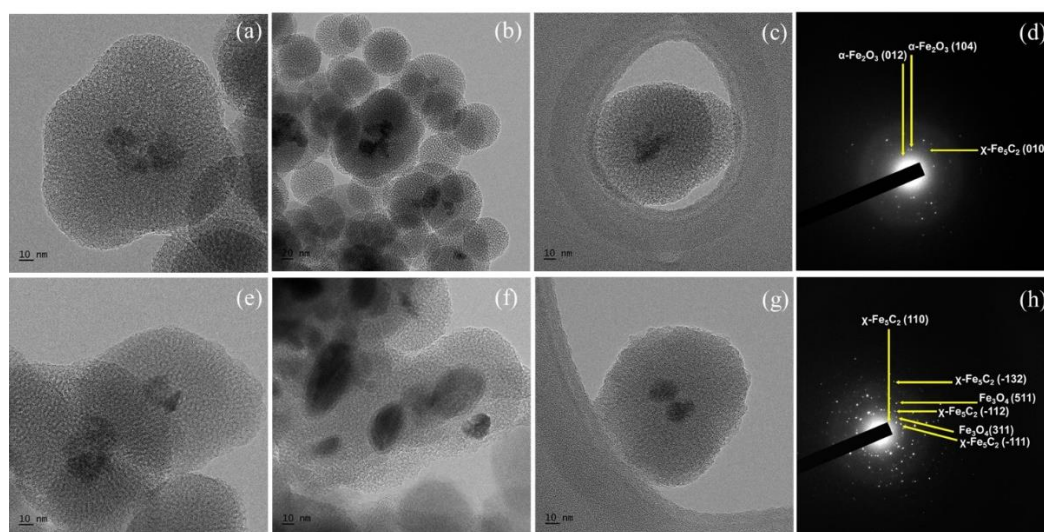


**Figure 3.** (a–c) TEM images and (d) SAED pattern of fresh  $\chi$ -Fe<sub>5</sub>C<sub>2</sub>@SiO<sub>2</sub>\_L catalyst; (e–g) TEM images and (h) SAED pattern of fresh  $\chi$ -Fe<sub>5</sub>C<sub>2</sub>@SiO<sub>2</sub>\_H catalyst.

The average crystallite size of  $\chi$ -Fe<sub>5</sub>C<sub>2</sub> in the  $\chi$ -Fe<sub>5</sub>C<sub>2</sub>@SiO<sub>2</sub>\_H catalyst calculated at  $2\theta = 39.4^\circ$  from the XRD result was 20.03 nm after the nanoparticles were encapsulated, indicating that the crystal size in the core was almost unchanged. To further verify the structure of the silica shell, N<sub>2</sub>-physisorption analysis was conducted on both catalysts. The N<sub>2</sub>-physisorption results of the  $\chi$ -Fe<sub>5</sub>C<sub>2</sub>@SiO<sub>2</sub>\_L catalyst are shown in Table S1. The BET surface area was 301 m<sup>2</sup>/g, and the average pore size and volume were 7.0 nm and 0.5 cm<sup>3</sup>/g, respectively. The N<sub>2</sub>-physisorption results of the  $\chi$ -Fe<sub>5</sub>C<sub>2</sub>@SiO<sub>2</sub>\_H catalyst are shown in Figure 4a,b. The BET surface area calculated from the adsorption isotherm in Figure 4a was 239 m<sup>2</sup>/g. The pore size distribution in Figure 4b shows a relatively sharp peak at ca. 2.3 nm and another broadened peak above 10 nm. The average pore size and pore volume were measured as 5.7 nm and 0.3 cm<sup>3</sup>/g, respectively. The pore volume at approximately 2.3 nm appeared to be small due to residue of PVP and CTAB still remaining after the synthesis. The result of SAXS of the  $\chi$ -Fe<sub>5</sub>C<sub>2</sub>@SiO<sub>2</sub>\_H catalyst in Figure 4c shows a slightly broadened peak at approximately 0.13 Å<sup>-1</sup>, and the pore structure could be considered similar to that of MCM-41 since the peak appears very similar to the reflection of the (100) plane of MCM-41 in terms of q vector and profile. The pores of the silica shell appeared to have a wormhole-like and short-range morphology, as shown in TEM images, and it could be corroborated by SAXS results that the pore structure seemed to be a partially ordered mesoporous structure; similar structures can be found in literature elsewhere [19,22–24]. The wall thickness of the pore structure was calculated using the d-spacing of the (100) plane and pore size from the N<sub>2</sub>-physisorption result. As the pore structure appeared to be similar to that of MCM-41, the calculation could be simplified by assuming a hexagonal structure. The distance a<sub>0</sub>, the distance between the centers of two adjacent pores, was calculated in the same way as Sibeko et al. proposed [25], and the value was 54.8 Å. As the average pore size considering only mesopores below 10 nm was 2.2 nm, as shown in Figure 4b, the wall thickness was 32.7 Å, which is a slightly higher value than that of MCM-41 from the literature [25] for comparison.

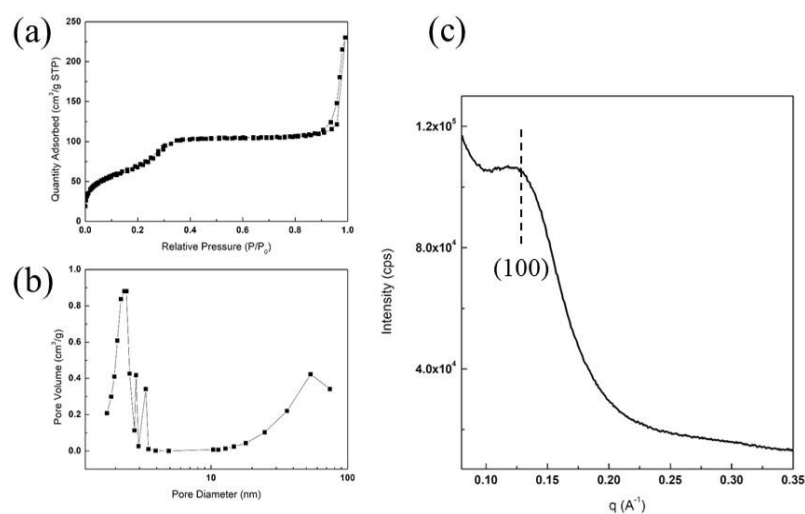


**Figure 4.** N<sub>2</sub>-physisorption and SAXS results: (a) N<sub>2</sub>-adsorption isotherm and (b) pore size distribution curve; (c) small-angle X-ray scattering pattern of fresh  $\chi$ -Fe<sub>5</sub>C<sub>2</sub>@SiO<sub>2</sub>\_H catalyst.

### 3.3. Activity Test Results

Figure 5 shows the catalytic performance of the catalysts, including CO conversion, product selectivity, and CO to CO<sub>2</sub> and hydrocarbon conversions. As the FTS active phase was directly synthesized, an in situ gaseous pre-treatment was not necessary before the reaction. The catalytic activity of the catalysts was evaluated at 300 °C and 10 bar in a micro fixed-bed reactor. The highest CO conversion over the  $\chi$ -Fe<sub>5</sub>C<sub>2</sub>@SiO<sub>2</sub>\_L catalyst was 10.8% at TOS 5.5 h and decreased to 7.4% at the end of the reaction. The low loading amount of the iron species and the phase transformation to  $\alpha$ -Fe<sub>2</sub>O<sub>3</sub> were believed to cause low Fischer–Tropsch synthesis performance. The confining geometry due to the encapsulation with porous silica was believed to play a protective role against deactivation, and the conversion and selectivities of products appeared steady. In addition, the light olefin ratio was higher than any other FTS reaction results in Table 1. The presence of the  $\theta$ -Fe<sub>3</sub>C phase in an iron-based catalyst is believed to affect the formation of light olefins, as reported in [26]. The generation of CO<sub>2</sub> was barely seen, whereas the consumption was observed at a very low rate, under 3%. The  $\alpha$ -Fe<sub>2</sub>O<sub>3</sub> phase is known to be the active phase for the reverse water–gas shift (RWGS) reaction [27], and the  $\theta$ -Fe<sub>3</sub>C phase is also known to be the active phase for CO<sub>2</sub> hydrogenation [28].

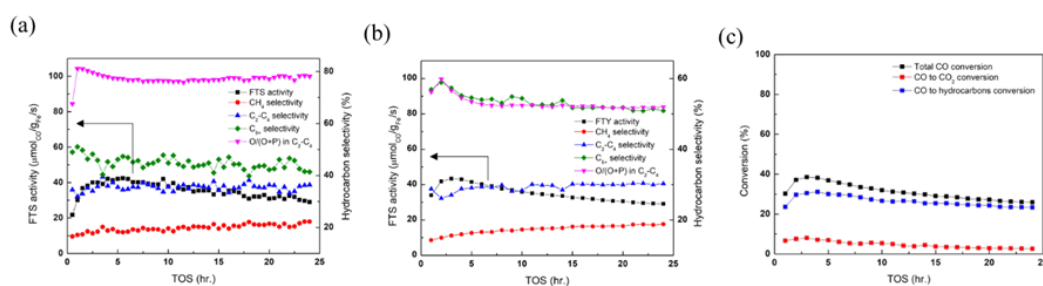


**Figure 5.** (a) The FTS reaction activity and hydrocarbon selectivity over the  $\chi$ -Fe<sub>5</sub>C<sub>2</sub>@SiO<sub>2</sub>\_L catalyst during the 24 h time on stream; (b) the FTS reaction activity and hydrocarbon selectivity over the  $\chi$ -Fe<sub>5</sub>C<sub>2</sub>@SiO<sub>2</sub>\_H catalyst during the 24 h time on stream; (c) CO conversions to hydrocarbons and CO<sub>2</sub> of the  $\chi$ -Fe<sub>5</sub>C<sub>2</sub>@SiO<sub>2</sub>\_H catalyst, the total CO conversion is the sum of the CO to hydrocarbon conversion and the CO to CO<sub>2</sub> conversion. Reaction conditions: 0.3 g catalyst, 300 °C, 10 bar, H<sub>2</sub>/CO = 2.1, GHSV = 4000 mL g<sub>cat</sub><sup>-1</sup>·h<sup>-1</sup>.

**Table 1.** CO conversion, CO<sub>2</sub> and hydrocarbon selectivity, and FTS activity of  $\chi$ -Fe<sub>5</sub>C<sub>2</sub>@SiO<sub>2</sub>\_L,  $\chi$ -Fe<sub>5</sub>C<sub>2</sub>@SiO<sub>2</sub>\_H, and other reference catalysts.

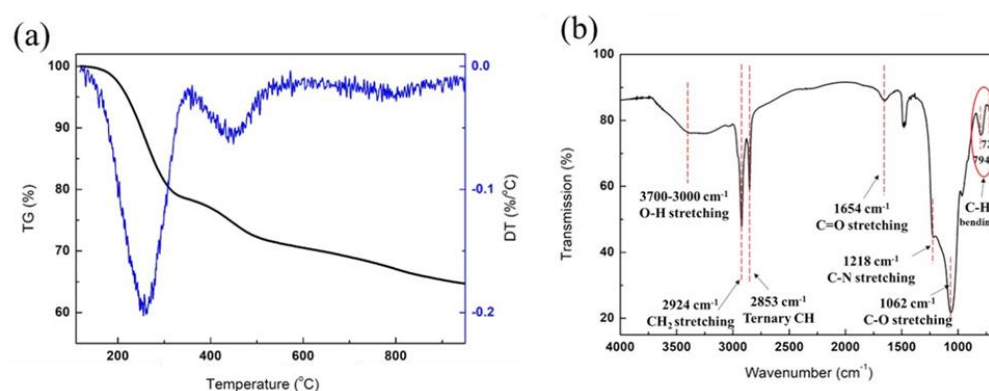
Catalyst	Fe Loading (wt.%)	CO conv. (%)	Hydrocarbon Selectivity (%)				CO <sub>2</sub> sel. (%)	FTS Activity ( $\mu\text{mol}_{\text{CO}}/\text{g}_{\text{Fe}}/\text{s}$ )	Reaction Condition	Ref.
			CH <sub>4</sub>	C <sub>2</sub> -C <sub>4</sub>	C <sub>5+</sub>	O/(O + P) in C <sub>2</sub> -C <sub>4</sub>				
$\chi$ -Fe <sub>5</sub> C <sub>2</sub> @SiO <sub>2</sub> _L	3.5	10.8	18.2	34.5	47.3	77.2	-	42.5	300 °C, 10 bar, H <sub>2</sub> /CO = 2.1, GHSV = 4000 mL·g <sub>cat</sub> <sup>-1</sup> ·h <sup>-1</sup>	This work
$\chi$ -Fe <sub>5</sub> C <sub>2</sub> @SiO <sub>2</sub> _H	12.2	38.5	15.6	27.1	57.3	56.6	20.9	44.1	300 °C, 10 bar, H <sub>2</sub> /CO = 2.1, GHSV = 4000 mL·g <sub>cat</sub> <sup>-1</sup> ·h <sup>-1</sup>	This work
FeSi-syn	50.9	22.3	12.9	17.1	70.0	47.6	2.8	7.2	260 °C, 30 bar, H <sub>2</sub> /CO = 2, GHSV = 4000 h <sup>-1</sup>	[13]
15.7Fe/AC	15.7	29.4	18.4	51.1	30.6	44.1	30.1	34.8	260 °C, 20.7 bar, H <sub>2</sub> /CO = 0.9, GHSV = 3000 mL·g <sub>cat</sub> <sup>-1</sup> ·h <sup>-1</sup>	[29]
Fe25Si	58.9	46.7	15.6	39.2	45.2	33.3	N.A.*	6.7	280 °C, 15 bar, H <sub>2</sub> /CO = 2, GHSV = 2000 mL·g <sub>cat</sub> <sup>-1</sup> ·h <sup>-1</sup>	[30]
CAT-H <sub>2</sub> O	54.5	46.5	11.7	25.9	62.4	N.A.*	30.0	36.0	280 °C, 20 bar, H <sub>2</sub> /CO = 1, GHSV = 12000 mL·g <sub>cat</sub> <sup>-1</sup> ·h <sup>-1</sup>	[31]
SiO <sub>2</sub> /α-Fe <sub>2</sub> O <sub>3</sub>	35.0	44.9	18.7	47.8	33.5	25.1	25.1	54.0	280 °C, 10 bar, H <sub>2</sub> /CO = 1, GHSV = 5000 mL·g <sub>cat</sub> <sup>-1</sup> ·h <sup>-1</sup>	[32]
Al <sub>2</sub> O <sub>3</sub> /α-Fe <sub>2</sub> O <sub>3</sub>	35.0	61.6	16.0	47.3	36.7	33.9	33.9	74.1	280 °C, 10 bar, H <sub>2</sub> /CO = 1, GHSV = 5000 mL·g <sub>cat</sub> <sup>-1</sup> ·h <sup>-1</sup>	[32]

\* N.A.: not available.

As indicated in Section 3.2, the preparation method was modified so that the Fe loading could be increased and phase transformation could be suppressed as much as possible, as mentioned in Section 2.2.2. In the reaction where the  $\chi$ -Fe<sub>5</sub>C<sub>2</sub>@SiO<sub>2</sub>\_H catalyst was used, the CO conversion was greatly enhanced and showed the highest conversion of 38.5%, and the FTS activity reached 44.1  $\mu\text{mol}_{\text{CO}}/\text{g}_{\text{Fe}}/\text{s}$  at TOS 3 h, as shown in Table 1. The degree of FTS activity was further investigated by a comparison with the results in the literature, and the FTS activity of this study appeared to be higher than or comparable to those from the references shown in Table 1. After TOS 3 h, the CO conversion gradually decreased. The overall CO conversion could be attributed to both FTS and water–gas shift (WGS), and the activity of WGS was assessed by CO to CO<sub>2</sub> conversion, as shown in Figure 5c. During the reaction, CO to CO<sub>2</sub> conversion consistently decreased, and the final value was measured at a significantly low level of approximately 2%, as shown in Figure 5c. The CO<sub>2</sub> selectivity was also relatively high in the early stage of the reaction, but decreased to a significantly low level to be 9.9% (not shown). This indicated that WGS activity was high at first but gradually decreased. If WGS activity was disregarded, the CO to hydrocarbon conversion (blue) shown in Figure 5c appeared to be steadier. More specifically, the CO to hydrocarbon conversion seemed greatly stabilized after TOS 10 h and decreased by only about 3.2 percentage points thereafter. It was believed that due to the absence of a calcination step in the catalyst preparation, H<sub>2</sub>O molecules and surface hydroxyl groups associated with the silica shell could have evolved during the reaction, and they seemed to influence WGS activity.

To identify the species and to assess the amounts of released molecules, TG/DTA analysis was performed, and the result is shown in Figure 6a. Two steps of thermal decomposition were shown in the TGA result. The first step was in the temperature range

of 150 °C to 360 °C, and this peak agreed with the decomposition peak of CTAB [33]. The second step ranging from 360 °C to 530 °C appeared to be in agreement with the temperature range of thermal decomposition of PVP [34]. The temperature range from 150 °C to 500 °C could be assigned to excess strongly bound water and surface hydroxyl groups [32]. TG/DTA analysis implied that the absence of a calcination step during the preparation of the catalyst caused insufficient removal of the surfactant and water. As mentioned, the evolution of water from the silica shell might have caused excessive WGS activity in the early stage of the reaction.



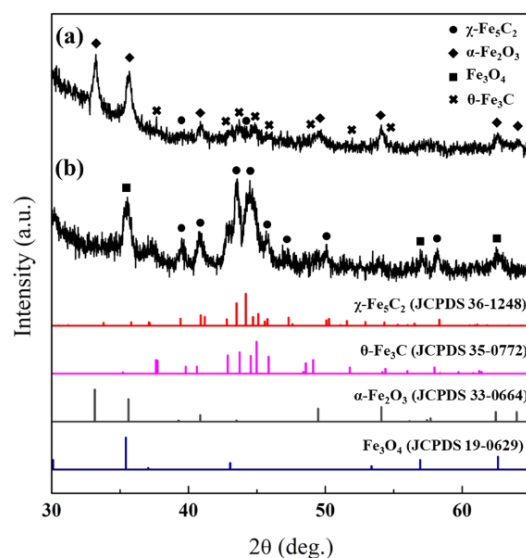
**Figure 6.** TG/DTA and FT-IR results: (a) TG/DTA result and (b) FTIR spectra of fresh  $\chi$ -Fe<sub>5</sub>C<sub>2</sub>@SiO<sub>2</sub>\_H catalyst.

Figure 6b shows the FT-IR spectra of the  $\chi$ -Fe<sub>5</sub>C<sub>2</sub>@SiO<sub>2</sub>\_H catalyst. The broad band at 3000 to 3700 cm<sup>-1</sup> was assigned to the characteristic bands for water molecules, surface hydroxyls, and hydroxyl functional groups from PVP. Other bands marked in Figure 6b correspond to the characteristic bands of functional groups included in the stabilizing agent, PVP [35]. This corroborated the result of TG/DTA and verified that the evolution of water and hydroxyls could cause WGS in the early stages of the reaction.

### 3.4. Characteristics of Spent Catalyst

The structure, morphology, and iron species of the spent catalysts were identified and analyzed by XRD, TEM, and Mössbauer emission spectroscopy (MES) methods. Figure 7 shows the XRD patterns of the spent catalysts. The  $\chi$ -Fe<sub>5</sub>C<sub>2</sub>,  $\theta$ -Fe<sub>3</sub>C, and  $\alpha$ -Fe<sub>2</sub>O<sub>3</sub> phases were observed in the spent  $\chi$ -Fe<sub>5</sub>C<sub>2</sub>@SiO<sub>2</sub>\_L. The kinds of phases were the same, but the amount of  $\chi$ -Fe<sub>5</sub>C<sub>2</sub> turned out to be decreased and possibly converted into oxidized phases since the peak at around 50° of  $\chi$ -Fe<sub>5</sub>C<sub>2</sub> was barely observed in this spent sample but was originally observed in the fresh catalyst as shown in Figure 2a. Similarly, the spent  $\chi$ -Fe<sub>5</sub>C<sub>2</sub>@SiO<sub>2</sub>\_H was shown to have the same kinds of phases such as  $\chi$ -Fe<sub>5</sub>C<sub>2</sub> and Fe<sub>3</sub>O<sub>4</sub>, which were the same phases contained in the fresh one. However, additional but slight oxidation or phase change to Fe<sub>3</sub>O<sub>4</sub> seemed to occur during the reaction because a new peak at  $2\theta = 56.9^\circ$  appeared.

The Fe 2p XPS spectra of the catalysts are shown in Figure S2. The peaks at binding energies of around 707 eV and 720 eV were allocated to Fe 2p 3/2 and Fe 2p 1/2 of the iron carbide phases, respectively [18]. The peaks situated at about 710 eV and 723 eV were attributed to the main peaks of iron oxide phases of the 2p 3/2 and 2p 1/2 regions, respectively [36,37]. All peaks were positioned at similar binding energies even after the FTS reaction.



**Figure 7.** XRD pattern of spent catalysts after reaction: (a)  $\chi$ -Fe<sub>5</sub>C<sub>2</sub>@SiO<sub>2</sub>\_L; (b)  $\chi$ -Fe<sub>5</sub>C<sub>2</sub>@SiO<sub>2</sub>\_H.

The average crystal size of  $\chi$ -Fe<sub>5</sub>C<sub>2</sub> in spent  $\chi$ -Fe<sub>5</sub>C<sub>2</sub>@SiO<sub>2</sub>\_L was very difficult to measure since there no overlapped peaks of the corresponding phase were observed. The average crystal size of  $\alpha$ -Fe<sub>2</sub>O<sub>3</sub> calculated at  $2\theta = 35.6^\circ$  was 23.8 nm, which is very close to that of the fresh catalyst (22.7 nm). Regarding the spent  $\chi$ -Fe<sub>5</sub>C<sub>2</sub>@SiO<sub>2</sub>\_H catalyst, the average crystal size of  $\chi$ -Fe<sub>5</sub>C<sub>2</sub> could be calculated by the Scherrer equation at  $2\theta = 39.4^\circ$ , and the size was 18.75 nm. The crystal size of the Fe<sub>3</sub>O<sub>4</sub> phase in this spent catalyst was calculated from the (311) diffraction peak using the Scherrer equation, and the crystal size barely changed from 11.85 nm to 12.81 nm. The encapsulation with a silica shell, especially with higher Fe loading, protected the iron carbide nanoparticles more effectively from sintering and re-oxidation, which are known to be the main causes of deactivation.

The TEM images and SAED patterns are shown in Figure 8. Figure 8a–c show the morphology of the spent  $\chi$ -Fe<sub>5</sub>C<sub>2</sub>@SiO<sub>2</sub>\_L catalyst, and the morphology of the catalyst was well maintained even after the FTS reaction. In addition, as the average crystallite size calculated with the XRD result did not change during the reaction, TEM images showed that the crystallite size of the iron nanoparticles was almost unchanged in the spent catalyst. In Figure 8d,  $\chi$ -Fe<sub>5</sub>C<sub>2</sub>,  $\theta$ -Fe<sub>3</sub>C, and  $\alpha$ -Fe<sub>2</sub>O<sub>3</sub> phases can be observed. Figure 8e–g show that the morphology of the catalyst after 24 h of FTS appeared sustained compared with that of the fresh  $\chi$ -Fe<sub>5</sub>C<sub>2</sub>@SiO<sub>2</sub>\_H catalyst. The SAED patterns in Figure 8h indicate that both the  $\chi$ -Fe<sub>5</sub>C<sub>2</sub> and Fe<sub>3</sub>O<sub>4</sub> phases were observed. Although sintering and phase transformation did not occur significantly during the exothermic reaction over the  $\chi$ -Fe<sub>5</sub>C<sub>2</sub>@SiO<sub>2</sub>\_H catalyst, slight deactivation was observed as shown in Figure 5c. The amorphous silica peak of the spent catalyst in Figure S3 shifted slightly to a larger  $2\theta$  value, compared with that of the fresh catalyst. The pore structure of the silica shell appeared to undergo thermal contraction because hydroxyls and decomposed molecules of chemical agents from the silica structure were eliminated during the reaction. This might be due to the removal of the calcination step during the preparation of encapsulated catalysts in order to avert phase change or oxidation of active iron carbide. To verify the structural change of the silica shell, the catalyst was characterized by N<sub>2</sub>-physisorption and SAXS analysis. The physisorption result of the spent  $\chi$ -Fe<sub>5</sub>C<sub>2</sub>@SiO<sub>2</sub>\_H catalyst is shown in Figure 9a,b. The BET surface area and the pore volume were greatly increased, as shown in Table S1, which could be the result of the elimination of CTAB and PVP and the condensation of small molecules such as water. The result of SAXS analysis in Figure 9c shows that the  $q$  vector for the (100) d-spacing of the ordered mesoporous fraction did not change after the reaction, indicating that the structural change of the ordered mesoporous fraction was slight, and the intensity increased owing to the elimination of CTAB, PVP, and water molecules associated with the silica shell.

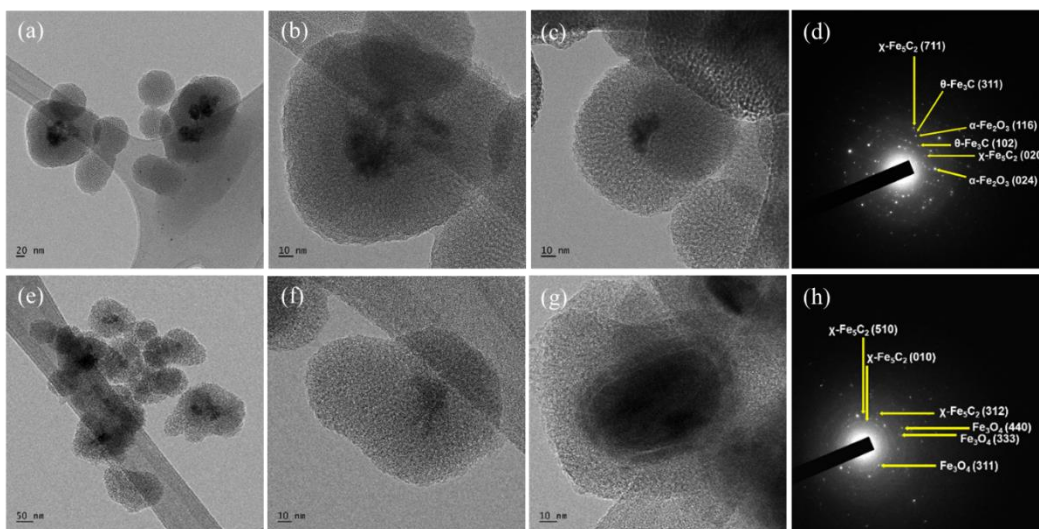


**Figure 8.** (a–c) TEM images and (d) SAED pattern of spent  $\chi$ -Fe<sub>5</sub>C<sub>2</sub>@SiO<sub>2</sub>\_L catalyst; and (e–g) TEM images and (h) SAED pattern of spent  $\chi$ -Fe<sub>5</sub>C<sub>2</sub>@SiO<sub>2</sub>\_H catalyst.

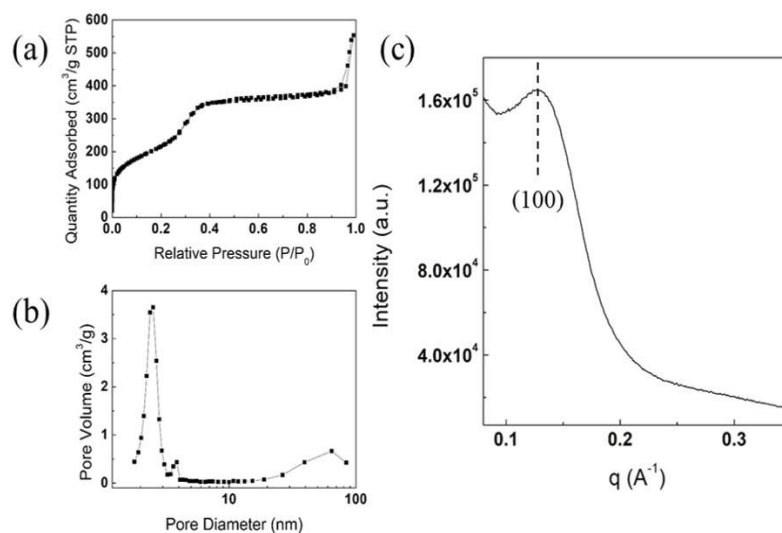


**Figure 9.** N<sub>2</sub>-physorption and SAXS results: (a) N<sub>2</sub>-adsorption isotherm and (b) pore size distribution curve; (c) small-angle X-ray scattering pattern of spent  $\chi$ -Fe<sub>5</sub>C<sub>2</sub>@SiO<sub>2</sub>\_H catalyst after reaction.

Mössbauer emission spectroscopy (MES) was conducted for identifying kinds and fractions of iron phases in  $\chi$ -Fe<sub>5</sub>C<sub>2</sub>@SiO<sub>2</sub> catalysts. MES results of fresh and spent  $\chi$ -Fe<sub>5</sub>C<sub>2</sub>@SiO<sub>2</sub> catalysts are shown in Figure 10, and the specific parameters are shown in Table 2. The MES spectra of  $\chi$ -Fe<sub>5</sub>C<sub>2</sub>@SiO<sub>2</sub>\_L showed two sextets for Fe<sub>3</sub>O<sub>4</sub>, three sextets for  $\chi$ -Fe<sub>5</sub>C<sub>2</sub>, one sextet for Fe<sub>3</sub>C, and one doublet in the catalyst regardless of evaluating the FTS reaction, as shown in Figure 10a,b. The doublet can be assigned to  $\alpha$ -Fe<sub>2</sub>O<sub>3</sub>, considering the XRD spectra shown in Figures 2a and 7a. By comparison of the relative areas of the fresh catalyst with those of the spent  $\chi$ -Fe<sub>5</sub>C<sub>2</sub>@SiO<sub>2</sub>\_L catalyst shown in Table 2, it can be seen that  $\chi$ -Fe<sub>5</sub>C<sub>2</sub> and Fe<sub>3</sub>C slightly decreased, Fe<sub>3</sub>O<sub>4</sub> decreased from 46.67% to 34.75%, and  $\alpha$ -Fe<sub>2</sub>O<sub>3</sub> increased from 7.78% to 21.09%.

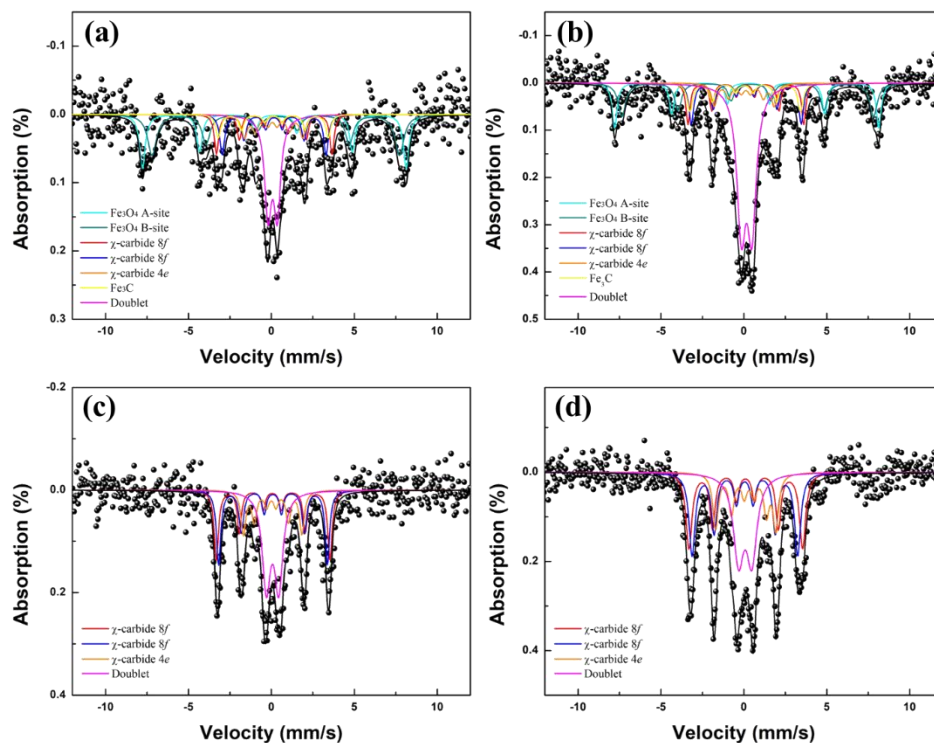


Figure 10. MES spectra of (a) fresh  $\chi$ -Fe<sub>5</sub>C<sub>2</sub>@SiO<sub>2</sub>\_L catalyst, (b) fresh  $\chi$ -Fe<sub>5</sub>C<sub>2</sub>@SiO<sub>2</sub>\_L catalyst, (c) fresh  $\chi$ -Fe<sub>5</sub>C<sub>2</sub>@SiO<sub>2</sub>\_H catalyst, and (d) spent  $\chi$ -Fe<sub>5</sub>C<sub>2</sub>@SiO<sub>2</sub>\_H catalyst.

Table 2. Mössbauer parameters of  $\chi$ -Fe<sub>5</sub>C<sub>2</sub>@SiO<sub>2</sub>\_L and  $\chi$ -Fe<sub>5</sub>C<sub>2</sub>@SiO<sub>2</sub>\_H catalysts.

Sample	$\delta^*$ (mm/s)	$\Delta E_Q$ (mm/s)	H <sub>hf</sub> (kOe)	phase	Area (%)	Composition (%)
$\chi$ -Fe <sub>5</sub> C <sub>2</sub> @SiO <sub>2</sub> _L	0.22	-0.04	493.8	Fe <sub>3</sub> O <sub>4</sub> (A)	21.39	46.67
	0.36	-0.04	463.1	Fe <sub>3</sub> O <sub>4</sub> (B)	25.28	
	0.13	0.04	216.3	$\chi$ -Fe <sub>5</sub> C <sub>2</sub> 8f	11.37	34.21
	0.16	0.0	190.4	$\chi$ -Fe <sub>5</sub> C <sub>2</sub> 8f	13.22	
	0.09	0.04	109.4	$\chi$ -Fe <sub>5</sub> C <sub>2</sub> 4e	9.62	
	0.11	0.0	205.9	Fe <sub>3</sub> C	11.34	11.34
	0.08	0.55	-	Doublet	7.78	7.78
Spent	0.22	-0.04	494.6	Fe <sub>3</sub> O <sub>4</sub> (A)	15.94	34.75
	0.33	-0.05	470.2	Fe <sub>3</sub> O <sub>4</sub> (B)	18.81	
	0.10	0.02	216.6	$\chi$ -Fe <sub>5</sub> C <sub>2</sub> 8f	11.72	33.50
	0.11	0.01	202.8	$\chi$ -Fe <sub>5</sub> C <sub>2</sub> 8f	13.07	
	0.09	0.04	112.3	$\chi$ -Fe <sub>5</sub> C <sub>2</sub> 4e	8.71	
	0.10	0.02	207.1	Fe <sub>3</sub> C	10.66	10.66
0.15	0.63	-	Doublet	21.09	21.09	
$\chi$ -Fe <sub>5</sub> C <sub>2</sub> @SiO <sub>2</sub> _H	0.08	0.00	214.4	$\chi$ -Fe <sub>5</sub> C <sub>2</sub> 8f	28.13	80.55
	0.09	0.0	195.3	$\chi$ -Fe <sub>5</sub> C <sub>2</sub> 8f	31.10	
	0.08	0.04	110.9	$\chi$ -Fe <sub>5</sub> C <sub>2</sub> 4e	21.32	19.45
	0.08	0.74	-	Doublet	19.45	
Spent	0.10	0.01	213.6	$\chi$ -Fe <sub>5</sub> C <sub>2</sub> 8f	30.09	86.50
	0.08	0.0	197.7	$\chi$ -Fe <sub>5</sub> C <sub>2</sub> 8f	33.62	
	0.17	-0.04	113.0	$\chi$ -Fe <sub>5</sub> C <sub>2</sub> 4e	22.79	13.50
	0.08	0.78	-	Doublet	13.50	

\*  $\delta$ : isomer shift,  $\Delta E_Q$ : quadrupole shift, H<sub>hf</sub>: hyperfine magnetic field.

MES spectra of  $\chi$ -Fe<sub>5</sub>C<sub>2</sub>@SiO<sub>2</sub>\_H were found to be quite different from those of  $\chi$ -Fe<sub>5</sub>C<sub>2</sub>@SiO<sub>2</sub>\_L. They exhibited only three sextets for  $\chi$ -Fe<sub>5</sub>C<sub>2</sub> and one doublet in the catalyst regardless of evaluating the FTS reaction, as shown in Figure 10c,d. The doublet could be assigned to Fe<sub>3</sub>O<sub>4</sub>, considering the XRD spectra shown in Figures 2b and 7b. The Fe<sub>3</sub>O<sub>4</sub> phase in the  $\chi$ -Fe<sub>5</sub>C<sub>2</sub>@SiO<sub>2</sub>\_H catalyst was shown in the form of one doublet instead of two sextets in the MES spectra because the average size of Fe<sub>3</sub>O<sub>4</sub> was quite small. Other iron species were not observed even though the catalyst went through 24 h of reaction. In the fresh catalyst, relative areas of  $\chi$ -Fe<sub>5</sub>C<sub>2</sub> and Fe<sub>3</sub>O<sub>4</sub> were estimated as 80.55% and 19.45%, respectively. Those were found to be 86.50% and 13.50%, respectively, in the spent catalyst, as shown in Table 2. Only a slight change in the area of the  $\chi$ -Fe<sub>5</sub>C<sub>2</sub> phase was observed for the spent catalyst, indicating that the encapsulating silica shell protected iron nanoparticles from re-oxidation and phase transformation to something else. Due to the surrounding restriction by tightly encapsulating silica shell, carbon atoms around the nanoparticle seemed to have difficulty in penetrating into the  $\chi$ -Fe<sub>5</sub>C<sub>2</sub> phase of the confined nanoparticle since it seemed very difficult to modify the original crystalline structure into another iron carbide structure with higher carbon content in such restricted surroundings. Furthermore, it seemed that internal carbon atoms of the  $\chi$ -Fe<sub>5</sub>C<sub>2</sub> phase had similar difficulty in leaching out. A similar report indicated that the  $\chi$ -Fe<sub>5</sub>C<sub>2</sub> phase was unchanged or slightly changed after the FTS reaction when the catalyst was prepared by the formation of iron oxalate dihydrate particles followed by hydrothermal treatment. The spent Fe<sub>5</sub>C<sub>2</sub>@C catalyst showed slight sintering, which was proved by the sharper diffraction peak of the XRD spectrum [38].

#### 4. Conclusions

Nanoparticles of the pure  $\chi$ -Fe<sub>5</sub>C<sub>2</sub> phase were successfully synthesized using a wet-chemical route, followed by encapsulation with a partially ordered mesoporous silica shell. By doing so, it was shown that the pre-treatment step in FTS reaction could be eliminated. Due to the silica shell's physical restriction of the nanoparticles, sintering seemed successfully suppressed, which was elucidated by XRD and TEM methods. Structural analysis by small angle X-ray scattering method showed that the protective silica shell had a partially ordered mesoporous structure with a short range. Wide-angle XRD results showed that the crystallite size of the active  $\chi$ -Fe<sub>5</sub>C<sub>2</sub> phase did not seem to significantly change during the reaction. Using MES and XRD methods, it was found that the composition and the phase of active  $\chi$ -Fe<sub>5</sub>C<sub>2</sub> seemed well maintained during such an exothermic FTS with water produced as a by-product at high temperature and pressure. The Fischer–Tropsch activity of  $\chi$ -Fe<sub>5</sub>C<sub>2</sub> in this study was comparable to or higher than those reported in previous studies. In addition, CO<sub>2</sub> selectivity was found to be very low after stabilization.

**Supplementary Materials:** The following supporting information can be downloaded at: <https://www.mdpi.com/article/10.3390/nano12203704/s1>, Figure S1: XRD result of  $\chi$ -Fe<sub>5</sub>C<sub>2</sub> nanoparticles.; Figure S2: XPS spectra of Fe 2p for  $\chi$ -Fe<sub>5</sub>C<sub>2</sub>@SiO<sub>2</sub> catalysts.; Figure S3: XRD results of fresh and spent  $\chi$ -Fe<sub>5</sub>C<sub>2</sub>@SiO<sub>2</sub>\_H catalysts.; Table S1: N<sub>2</sub>-physisorption results of fresh and spent  $\chi$ -Fe<sub>5</sub>C<sub>2</sub>@SiO<sub>2</sub> catalysts.

**Author Contributions:** Conceptualization, S.C. and H.K.; writing, S.C. and K.-S.H.; methodology, H.K.; investigation, S.C. and K.-S.H.; MES analysis, H.C. and C.S.K.; supervision, review, and editing, K.-S.H. All authors have read and agreed to the published version of the manuscript.

**Funding:** This work was financially supported by a Korea Institute of Energy Technology Evaluation and Planning (KETEP) grant funded by the Korean government (MOTIE) (20214000000500, training program of CCUS for green growth) and also supported by the National Research Foundation of Korea (NRF-2019M3F4A1073044).

**Data Availability Statement:** The supplementary materials file above is available at the *Nanomaterials* website.

**Conflicts of Interest:** The authors declare no conflict of interest.

## References

1. Dry, M.E. The Fischer–Tropsch process: 1950–2000. *Catal. Today* **2002**, *71*, 227–241. [[CrossRef](#)]
2. Dry, M.; Steynberg, A. Commercial FT process applications. In *Studies in Surface Science and Catalysis*; Elsevier: Amsterdam, The Netherlands, 2004; Volume 152, pp. 406–481.
3. Dry, M.E. Present and future applications of the Fischer–Tropsch process. *Appl. Catal. A-Gen.* **2004**, *1*, 1–3. [[CrossRef](#)]
4. de Smit, E.; Weckhuysen, B.M. The renaissance of iron-based Fischer–Tropsch synthesis: On the multifaceted catalyst deactivation behaviour. *Chem. Soc. Rev.* **2008**, *37*, 2758–2781. [[CrossRef](#)]
5. Abelló, S.; Montané, D. Exploring Iron-based Multifunctional Catalysts for Fischer–Tropsch Synthesis: A Review. *Chem. Sus. Chem.* **2011**, *4*, 1538–1556. [[CrossRef](#)]
6. Zhang, C.; Jun, K.W.; Ha, K.S.; Lee, Y.J.; Kang, S.C. Efficient utilization of greenhouse gases in a gas-to-liquids process combined with CO<sub>2</sub>/steam-mixed reforming and Fe-based Fischer–Tropsch synthesis. *Environ. Sci. Technol.* **2014**, *48*, 8251–8257. [[CrossRef](#)] [[PubMed](#)]
7. Pham, T.H.; Qi, Y.; Yang, J.; Duan, X.; Qian, G.; Zhou, X.; Chen, D.; Yuan, W. Insights into Hägg Iron-Carbide-Catalyzed Fischer–Tropsch Synthesis: Suppression of CH<sub>4</sub> Formation and Enhancement of C–C Coupling on  $\chi$ -Fe<sub>5</sub>C<sub>2</sub> (510). *ACS Catal.* **2015**, *5*, 2203–2208. [[CrossRef](#)]
8. Yang, C.; Zhao, H.; Hou, Y.; Ma, D. Fe<sub>5</sub>C<sub>2</sub> nanoparticles: A facile bromide-induced synthesis and as an active phase for Fischer–Tropsch synthesis. *J. Am. Chem. Soc.* **2012**, *134*, 15814–15821. [[CrossRef](#)]
9. Sarkar, A.; Seth, D.; Dozier, A.K.; Neathery, J.K.; Hamdeh, H.H.; Davis, B.H. Fischer–Tropsch synthesis: Morphology, phase transformation and particle size growth of nano-scale particles. *Catal. Lett.* **2007**, *117*, 1–17. [[CrossRef](#)]
10. Pendyala, V.R.R.; Graham, U.M.; Jacobs, G.; Hamdeh, H.H.; Davis, B.H. Fischer–Tropsch Synthesis: Morphology, Phase Transformation, and Carbon-Layer Growth of Iron-Based Catalysts. *ChemCatChem* **2014**, *6*, 1952–1960. [[CrossRef](#)]
11. Bukur, D.B.; Okabe, K.; Rosynek, M.P.; Li, C.; Wang, D.; Rao, K.; Huffman, G. Activation studies with a precipitated iron catalyst for Fischer–Tropsch synthesis: I. Characterization studies. *J. Catal.* **1995**, *155*, 353–365. [[CrossRef](#)]
12. Chernavskii, P.; Kazak, V.; Pankina, G.; Ordonsky, V.; Khodakov, A. Mechanistic Aspects of the Activation of Silica-Supported Iron Catalysts for Fischer–Tropsch Synthesis in Carbon Monoxide and Syngas. *ChemCatChem* **2016**, *8*, 390–395. [[CrossRef](#)]
13. Chang, Q.; Zhang, C.; Liu, C.; Wei, Y.; Cheruvathur, A.V.; Dugulan, A.I.; Niemantsverdriet, J.; Liu, X.; He, Y.; Qing, M. Relationship between iron carbide phases ( $\epsilon$ -Fe<sub>2</sub>C, Fe<sub>7</sub>C<sub>3</sub>, and  $\chi$ -Fe<sub>5</sub>C<sub>2</sub>) and catalytic performances of Fe/SiO<sub>2</sub> Fischer–Tropsch catalysts. *ACS Catal.* **2018**, *8*, 3304–3316. [[CrossRef](#)]
14. Ding, M.; Yang, Y.; Li, Y.; Wang, T.; Ma, L.; Wu, C. Impact of H<sub>2</sub>/CO ratios on phase and performance of Mn-modified Fe-based Fischer Tropsch synthesis catalyst. *Appl. Energy* **2013**, *112*, 1241–1246. [[CrossRef](#)]
15. de Smit, E.; Cinquini, F.; Beale, A.M.; Safonova, O.V.; van Beek, W.; Sautet, P.; Weckhuysen, B.M. Stability and reactivity of  $\epsilon$ – $\chi$ – $\theta$  iron carbide catalyst phases in Fischer–Tropsch synthesis: Controlling  $\mu$ C. *J. Am. Chem. Soc.* **2010**, *132*, 14928–14941. [[CrossRef](#)] [[PubMed](#)]
16. Yao, S.Y.; Yang, C.; Zhao, H.B.; Li, S.W.; Lin, L.L.; Wen, W.; Liu, J.X.; Hu, G.; Li, W.X.; Hou, Y.L.; et al. Reconstruction of the Wet Chemical Synthesis Process: The Case of Fe<sub>5</sub>C<sub>2</sub> Nanoparticles. *J. Phys. Chem. C* **2017**, *121*, 5154–5160. [[CrossRef](#)]
17. Tang, L.; He, L.; Wang, Y.; Chen, B.; Xu, W.; Duan, X.; Lu, A.-H. Selective fabrication of  $\chi$ -Fe<sub>5</sub>C<sub>2</sub> by interfering surface reactions as a highly efficient and stable Fischer–Tropsch synthesis catalyst. *Appl. Catal. B-Environ.* **2021**, *284*, 119753. [[CrossRef](#)]
18. Lee, H.K.; Lee, J.H.; Seo, J.H.; Chun, D.H.; Kang, S.W.; Lee, D.W.; Yang, J.I.; Rhim, G.B.; Youn, M.H.; Jeong, H.D.; et al. Extremely productive iron-carbide nanoparticles on graphene flakes for CO hydrogenation reactions under harsh conditions. *J. Catal.* **2019**, *378*, 289–297. [[CrossRef](#)]
19. Karandikar, P.R.; Lee, Y.-J.; Kwak, G.; Woo, M.H.; Park, S.-J.; Park, H.-G.; Ha, K.-S.; Jun, K.-W. Co<sub>3</sub>O<sub>4</sub>@ Mesoporous Silica for Fischer–Tropsch Synthesis: Core–Shell Catalysts with Multiple Core Assembly and Different Pore Diameters of Shell. *J. Phys. Chem. C* **2014**, *118*, 21975–21985. [[CrossRef](#)]
20. Li, Q.; Kartikowati, C.W.; Horie, S.; Ogi, T.; Iwaki, T.; Okuyama, K. Correlation between particle size/domain structure and magnetic properties of highly crystalline Fe<sub>3</sub>O<sub>4</sub> nanoparticles. *Sci. Rep.* **2017**, *7*, 9894. [[CrossRef](#)]
21. Ahmadpoor, F.; Shojaosadati, S.A.; Delavari, H.H.; Christiansen, G.; Saber, R. Synthesis of Fe<sub>5</sub>C<sub>2</sub>@SiO<sub>2</sub> core@shell nanoparticles as a potential candidate for biomedical application. *Mater. Res. Express* **2018**, *5*, 55038. [[CrossRef](#)]
22. Kim, D.; Jeon, J.; Lee, W.; Lee, J.; Ha, K.S. Effective suppression of deactivation by utilizing Ni-doped ordered mesoporous alumina-supported catalysts for the production of hydrogen and CO gas mixture from methane. *Int. J. Hydrogen Energy* **2017**, *42*, 24744–24756. [[CrossRef](#)]
23. Tanev, P.T.; Pinnavaia, T.J. A neutral templating route to mesoporous molecular sieves. *Science* **1995**, *267*, 865–867. [[CrossRef](#)] [[PubMed](#)]
24. Prouzet, E.; Pinnavaia, T.J. Assembly of mesoporous molecular sieves containing wormhole motifs by a nonionic surfactant pathway: Control of pore size by synthesis temperature. *Angew. Chem. Int. Ed.* **1997**, *36*, 516–518. [[CrossRef](#)]
25. Sibeko, M.A.; Saladino, M.L.; Luyt, A.S.; Caponetti, E. Morphology and properties of poly(methyl methacrylate) (PMMA) filled with mesoporous silica (MCM-41) prepared by melt compounding. *J. Mater. Sci.* **2016**, *51*, 3957–3970. [[CrossRef](#)]
26. Liu, Y.; Chen, J.F.; Bao, J.; Zhang, Y. Manganese-Modified Fe<sub>3</sub>O<sub>4</sub> Microsphere Catalyst with Effective Active Phase of Forming Light Olefins from Syngas. *ACS Catal.* **2015**, *5*, 3905–3909. [[CrossRef](#)]

27. Gu, M.; Dai, S.; Qiu, R.; Ford, M.E.; Cao, C.; Wachs, I.E.; Zhu, M. Structure–activity relationships of copper-and potassium-modified iron oxide catalysts during reverse water–gas shift reaction. *ACS Catal.* **2021**, *11*, 12609–12619. [[CrossRef](#)]
28. Zhang, Y.L.; Fu, D.L.; Liu, X.L.; Zhang, Z.P.; Zhang, C.; Shi, B.F.; Xu, J.; Han, Y.F. Operando Spectroscopic Study of Dynamic Structure of Iron Oxide Catalysts during CO<sub>2</sub> Hydrogenation. *Chemcatchem* **2018**, *10*, 1272–1276. [[CrossRef](#)]
29. Ma, W.; Kugler, E.L.; Dadyburjor, D.B. Potassium effects on activated-carbon-supported iron catalysts for Fischer–Tropsch synthesis. *Energy Fuels* **2007**, *21*, 1832–1842. [[CrossRef](#)]
30. Suo, H.; Wang, S.; Zhang, C.; Xu, J.; Wu, B.; Yang, Y.; Xiang, H.; Li, Y.-W. Chemical and structural effects of silica in iron-based Fischer–Tropsch synthesis catalysts. *J. Catal.* **2012**, *286*, 111–123. [[CrossRef](#)]
31. Perez, S.; Mondragon, F.; Moreno, A. Iron ore as precursor for preparation of highly active  $\chi$ -Fe<sub>5</sub>C<sub>2</sub> core-shell catalyst for Fischer-Tropsch synthesis. *Appl. Catal. A-Gen.* **2019**, *587*, 117264. [[CrossRef](#)]
32. Lu, F.X.; Chen, X.; Lei, Z.G.; Wen, L.X.; Zhang, Y. Revealing the activity of different iron carbides for Fischer-Tropsch synthesis. *Appl. Catal. B-Environ.* **2021**, *281*, 119521. [[CrossRef](#)]
33. Wu, S.-H.; Chen, D.-H. Synthesis of high-concentration Cu nanoparticles in aqueous CTAB solutions. *J. Colloid Interfaces Sci.* **2004**, *273*, 165–169. [[CrossRef](#)] [[PubMed](#)]
34. Saroj, A.L.; Singh, R.K.; Chandra, S. Studies on polymer electrolyte poly(vinyl) pyrrolidone (PVP) complexed with ionic liquid: Effect of complexation on thermal stability, conductivity and relaxation behaviour. *Mater. Sci. Eng. B* **2013**, *178*, 231–238. [[CrossRef](#)]
35. Safo, I.A.; Werheid, M.; Dosche, C.; Oezaslan, M. The role of polyvinylpyrrolidone (PVP) as a capping and structure-directing agent in the formation of Pt nanocubes. *Nanoscale Adv.* **2019**, *1*, 3095–3106. [[CrossRef](#)]
36. Mousavi, M.; Habibi-Yangjeh, A.; Seifzadeh, D.; Nakata, K.; Vadivel, S. Exceptional photocatalytic activity for g-C<sub>3</sub>N<sub>4</sub> activated by H<sub>2</sub>O<sub>2</sub> and integrated with Bi<sub>2</sub>S<sub>3</sub> and Fe<sub>3</sub>O<sub>4</sub> nanoparticles for removal of organic and inorganic pollutants. *Adv. Powder Technol.* **2019**, *30*, 524–537. [[CrossRef](#)]
37. Hu, C.Q.; Gao, Z.H.; Yang, X.R. Fabrication and magnetic properties of Fe<sub>3</sub>O<sub>4</sub> octahedra. *Chem. Phys. Lett.* **2006**, *429*, 513–517. [[CrossRef](#)]
38. Hong, S.Y.; Chun, D.H.; Yang, J.-I.; Jung, H.; Lee, H.-T.; Hong, S.; Jang, S.; Lim, J.T.; Kim, C.S.; Park, J.C. A new synthesis of carbon encapsulated Fe<sub>5</sub>C<sub>2</sub> nanoparticles for high-temperature Fischer–Tropsch synthesis. *Nanoscale* **2015**, *7*, 16616–16620. [[CrossRef](#)]